

LLOL: Low-Latency Odometry for Spinning Lidars

Chao Qu, Shreyas S. Shivakumar, Wenxin Liu and Camillo J. Taylor

Abstract—In this paper, we present a low-latency odometry system designed for spinning lidars. Many existing lidar odometry methods wait for an entire sweep from the lidar before processing the data. This introduces a large delay between the first laser firing and its pose estimate. To reduce this latency, we treat the spinning lidar as a streaming sensor and process packets as they arrive. This effectively distributes expensive operations across time, resulting in a very fast and lightweight system with a much higher throughput and lower latency. Our open source implementation is available at <https://github.com/versatran01/llol>.

I. INTRODUCTION

Light Detection and Ranging (lidar) sensors are one of the primary sensing modalities in autonomous driving and robotics applications. They work by sweeping one or more laser beams through the scene and calculate range by measuring time of flight. This is apparent in mechanical lidars that continually spin a comb of lasers. However, solid-state lidars designed to minimize moving parts also involve redirecting a laser beam over time to cover a wider field of view (FOV).

Many existing lidar odometry systems wait for the lidar to complete a full revolution and then process the resulting sweep to update ego-motion along with any associated scene representations. Because of this, systems that combine Inertial Measurement Units (IMUs), cameras and lidars often accept that lidar is the slowest sensor in the system, and design algorithms based on that assumption [1], [2], [3]. At first glance this is a valid assumption since a spinning lidar usually rotates at 10 Hz, which is a much lower rate compared to those of a typical IMU (>100 Hz) or camera (>20 Hz). However, this data capture delay is an abstraction of the underlying mechanism of the lidar, and is adopted only for ease of processing. It ignores the streaming nature of the sensor and the fact that the raw lidar packets usually arrive at a much higher rate (>600 Hz). Recent works have also demonstrated that directly operating on lidar packets enables low-latency object detection, which is critical for autonomous driving [4], [5].

In this paper we show how to exploit this continuous stream of data to significantly decrease latency and increase throughput for lidar odometry. Fig. 1 shows the difference in latency of a standard lidar odometry and the one proposed in this paper. Consider the latency between the time of the

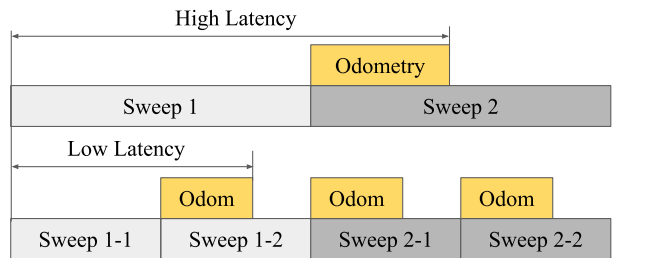


Fig. 1: Difference in latency when using full sweep (top) vs partial sweeps (bottom) in an odometry system. Gray blocks denote lidar acquisition time, and yellow blocks denote odometry runtime. We propose to process partial sweeps which allows the system to produce odometry at a higher rate with lower latency.

laser firing at the beginning of the sweep and the time that the sweep trajectory is estimated, we note that it has two components: the integration time of the lidar and the runtime of the odometry. By this definition, a system that operates on a full sweep will have twice the latency compared to one that operates on half a sweep.

Our proposed approach has two advantages. Firstly it can process partial sweeps by employing a circular buffer of range measurements which drastically increases the rate at which we can produce new pose measurements, for example our approach can produce pose estimates at a rate of 80Hz from a lidar sensor with a sweep rate of 10Hz. Secondly our approach can process the resulting range information extremely efficiently on modern processor architectures without the need for GPU acceleration which minimizes the latency of those pose estimates. Both of these properties, increased throughput and decreased latency, are particularly important in contexts where the pose estimates are being used for closed loop control of dynamic platforms like quadrotors.

In the rest of this paper, we describe key elements of our system in Section III and provide implementation details in Section IV. We then evaluate its accuracy and runtime by comparing to a state-of-the-art lidar odometry system [6] in Section V. We establish that by using partial sweeps we can increase the throughput substantially while lowering the effective latency. We show that by adopting a data-oriented design with array-based data structures, our system exhibits almost linear scalability in terms of multi-threading performance. Unfortunately, many popular datasets only provide lidar data pre-packaged as point clouds from full sweeps. Therefore, we also collected our own dataset to further validate our method. Our system, named LLOL, is open

We gratefully acknowledge the support of Distributed and Collaborative Intelligent Systems and Technology Collaborative Research Alliance (DCIST) and C-BRIC, a Semiconductor Research Corporation Joint University Microelectronics Program, program cosponsored by DARPA.

C. Qu, S. S. Shivakumar, W. Liu and C. J. Taylor are with the GRASP Laboratory, School of Engineering and Applied Sciences, University of Pennsylvania {quchao, sshreyas, wenxinl, cjtaylor}@seas.upenn.edu

sourced and available to the community.

II. RELATED WORK

In this section, we review related work on lidar-(inertial) odometry with a particular focus on systems that have been demonstrated to run in real time on embedded platforms.

A. Lidar Odometry

In a seminal paper Zhang *et al.* proposed LOAM, a feature based lidar odometry designed to work on embedded platforms, with loose IMU integration and a discrete trajectory representation [7]. Shan *et al.* improved LOAM for ground robots by leveraging an initial segmentation procedure to detect ground planes [8]. LOAM was further extended by Lin *et al.* to work with limited **FOV** LiDARs, supporting irregular sampling of feature points and enhanced outlier rejection. Liu *et al.* proposed a method of local bundle adjustment and a temporal sliding window that allows for real-time performance while also improving odometry, and use LOAM as a front end in their validation [9]. Elastic-Fusion, SuMa and MARS use a surfel based map to improve performance, and allow representation of larger scale environments [10], [11], [12], [13]. Palieri *et al.* proposed LOCUS, a multi-sensor lidar-centric system for odometry and mapping that is robust to intermittent sensor degradation, and deployed it on both legged and wheeled robot platforms. Yokozuka *et al.* proposed LITAMIN [14], which is a light-weight lidar odometry. They adopt a voxelization step to reduce the number of points used in ICP and employ a modified GICP [15] cost that avoids expensive eigen-decomposition computations commonly used with the point-to-plane metric. LITAMIN2 further improves real-time performance by matching two distributions via a symmetric KL-divergence cost [16].

B. Lidar-inertial Odometry

Neuhaus *et al.* propose MC2SLAM, which is a tightly-coupled odometry system that is designed with real-time performance in mind. They report a runtime of approximately 60 ms, excluding an intermittent pose graph optimization step that requires an additional 108 ms every five frames. In [17], the authors propose LiLi-OM to address the irregular scan pattern of the Livox **lidar** similar to [18]. They perform tightly coupled lidar-inertial fusion with a keyframe-based sliding window optimization. They report a runtime performance of roughly 85 ms per sweep on Velodyne lidar data. LIO-SAM [19] improves upon [20] and uses a window of local sweeps instead of matching individual lidar sweeps to a global map. They report an improvement in efficiency and accuracy, and a runtime performance of roughly 50 ms-100 ms per sweep on a laptop CPU. Xu *et al.* proposed Fast-LIO and Fast-LIO2, which we use in our quantitative comparisons given their focus on real-time performance and support for similar hardware as our method [21], [6]. Fast-LIO2 achieves real-time performance on embedded CPUs via the use of an incremental KD Tree and tightly-couples **IMU** data. Perhaps the most similar work to ours is UPSLAM [22], which uses a union of depth panoramas [23] as its map

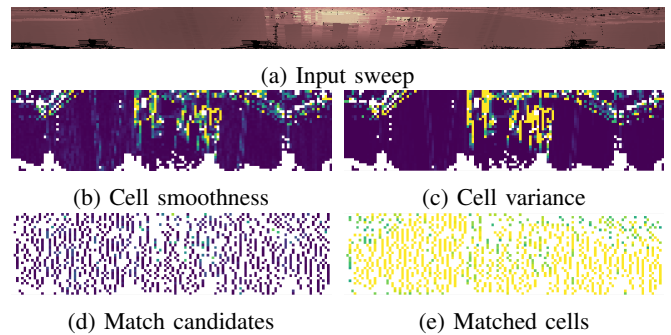


Fig. 2: Various stages in the feature detection process. Brighter color denotes higher value in both colormaps.

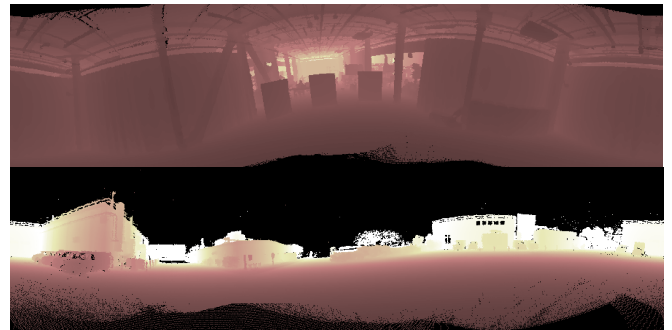


Fig. 3: Depth panoramas generated by our system for both indoor (top) and outdoor (bottom) scenes using the same resolution (256×1024) with a 90° vertical **FOV**.

representation. It is also a full-fledged SLAM system that includes loop closure. However, UPSLAM requires a GPU since it utilizes all points from a lidar sweep.

III. METHOD

A spinning **lidar** sensor produces data in packets which can be decoded by a driver to produce a final point cloud. It can also be converted into a spherical coordinate system resulting in a range image. In this work, we define a lidar **sweep** to be either a point cloud or a range image generated from a complete revolution of the sensor.

Our system consumes lidar packets directly and accumulates a partial sweep as a range image internally (Fig. 2a). Compared with structured point clouds, range images are more compact and memory efficient. Once the partial sweep reaches a desired integration time, the odometry system processes and produces a pose estimate. For ease of illustration, we assume a full sweep as input in this section. We address how to adapt our system to partial sweeps in section IV.

A. Feature Detection

The input to our system is a range image from which we can recover the 3D position of each pixel. There is usually too much information to process, as a typical lidar sweep consists of $64 \times 1024 = 65536$ data points. To reduce the amount of information, we divide the sweep into a grid of 2D cells and compute smoothness (2b) and variance (2c) for

each cell. Similar to [8], smoothness s is defined as

$$s = \frac{1}{|C|} \left| \sum_{n \in C} \frac{r_n}{r_m} - 1 \right| \quad (1)$$

where r_n is the range of pixel n , r_m is the range of the midpoint and $|C|$ is the number of valid pixels in cell C .

We then filter the entire grid by a maximum smoothness and variance threshold to identify planar regions in the sweep. An optional non-minimum suppression can be applied to further reduce the number of cells while maintaining a uniform distribution across the grid. We represent each remaining cell (2d) with a multivariate Gaussian with mean $\mu^S \in \mathbb{R}^3$ and covariance $\Sigma^S \in \mathbb{R}^{3 \times 3}$ which captures the statistics of the 3D positions of the points in that cell. These quantities will be used for data association and optimization. This feature detection stage is similar to the voxelization step in LITAMIN2 [16] but is carried out in the 2D image space.

B. Local Map Representation

Following UPSLAM [22], we employ a depth **panorama** (**pano**) [23] as our local map. A **pano** is similar to a sweep, but with higher resolution and represents the 3D structure at one point along the sensors trajectory. It is built by fusing multiple localized and motion-corrected sweeps. Compared with 3D map representations like point clouds or voxel/surfel grids, a depth **pano** has a fixed storage complexity. The advantages include low memory footprint, linear access patterns and adaptive spatial resolution. As shown in Fig. 3, the same **pano** size can be used to model both indoor and outdoor scenes. Whereas with 3D representations, one has to choose a suitable spatial resolution to voxelize the workspace, which results in high variance in runtime efficiency.

Due to its fixed viewpoint and spherical projection model, our **pano** map is susceptible to occlusions and limited horizontal **FOV**. In practice, we found this to be less of a problem since most of our robots move in open space with planar motions. Note that a graph of **panos** can be used for pose graph optimization to reduce drift [22], or fed into other loop closure systems [24], [25].

C. Local Trajectory Representation

At any given time, we maintain a local trajectory of the current sweep, which has a time span of $[t_0, t_1]$. It consists of a set of discrete states, each for a single column of cells in the grid. Given the laser firing time Δt , we can recover the column time by $t_c = t_0 + c \cdot \Delta t$. Each state $X_{S_t}^P$ consists of the position, velocity and orientation of the sensor at time $t \in [t_0, t_1]$ with respect to the current **pano** frame

$$X_{S_t}^P = [p_{S_t}^P \quad v_{S_t}^P \quad R_{S_t}^P] \quad (2)$$

Given a new sweep, we start from the last state of the previous sweep and propagate forward in time using the available **IMU** readings to obtain an initial guess. This trajectory estimate is then used to resolve the locations of the features in the sweep.

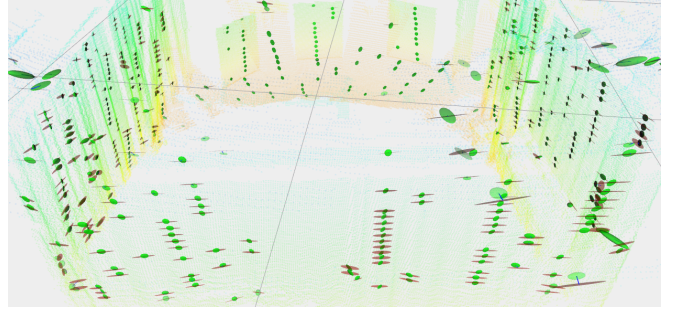


Fig. 4: Data association between sweep and pano. Red and green ellipsoids depict the normal distributions of grid cells and their matching windows in the **pano**.

D. Projective ICP

Given a set of match candidates (planar cells from III-A), we can estimate the pose of the current sweep by aligning it to the **pano** via an **Iterative closest point (ICP)** procedure.

1) *Data Association*: We find correspondences by projective data association [26], where points in the sweep frame \mathcal{S} are transformed into the **pano** frame \mathcal{P}

$$u^P = \pi(T_S^P \mu^S) = \pi(R_S^P \mu^S + p_S^P), \quad (3)$$

Here μ^S is the mean position of the cell from the sweep and u^P is its target pixel coordinate in the **pano**. $\pi(\cdot)$ is the spherical projection function, and $T_S^P \in \mathbb{SE}(3)$ is the rigid transformation from the sweep to the **pano** frame. We only accept matches that pass the following checks: 1) the target pixel must lie within the **pano**, 2) the depths of the target pixel and sweep point must be close enough, and 3) more than half of the pixels within a window around the target must be valid. These criteria will eliminate most of the outliers due to occlusion. The remaining ones can be handled by either a robust loss function or χ -squared test. We summarize the target pixel with a multivariate Gaussian with mean $\mu^P \in \mathbb{R}^3$ and covariance $\Sigma^P \in \mathbb{R}^{3 \times 3}$ using all valid pixels in the window.

2) *Pose Optimization*: Once the correspondences are established, as shown in Fig. 4, we proceed to the registration step. We employ the GICP [15] cost function in the optimization procedure,

$$r^2 = \|\mu^P - T_S^P \mu^S\|_{\Sigma}^2, \quad \Sigma = \Sigma^P + R_S^P \Sigma^S R_S^S \quad (4)$$

where $\|\cdot\|_{\Sigma}$ is the Mahalanobis distance and Σ^P and Σ^S are the covariance matrices in the sweep and **pano** frame respectively. When **IMU** data is available, we add an **IMU** preintegration factor [27] to constrain the start and the end state of the local trajectory. The error state parameters we wish to optimize represent a small correction $\Delta T_{\mathcal{P}}^{P'}$ in the **pano** frame such that the new state $X_{S_t}^{P'}$ can be updated via

$$T_{S_t}^{P'} = \Delta T_{\mathcal{P}}^{P'} \cdot T_{S_t}^P, \quad v_{S_t}^{P'} = v_{S_t}^P + \Delta p_{\mathcal{P}}^{P'} / \Delta t \quad (5)$$

where $\Delta p_{\mathcal{P}}^{P'}$ is the translation part of $\Delta T_{\mathcal{P}}^{P'}$ and $\Delta t = t_1 - t_0$. After a few iterations of the Levenberg-Marquardt procedure, the resulting update is applied to the starting state of the

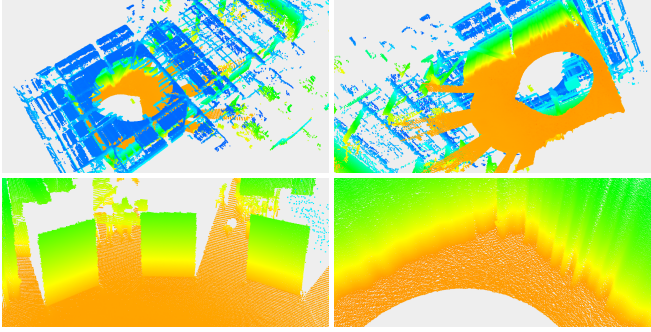


Fig. 5: An indoor space (top) mapped with our lidar odometry. The points are generated by back-projecting a depth panorama. Details of the scene (bottom) are faithfully preserved by the depth panorama.

sweep trajectory. We then repropagate the entire trajectory and update correspondences for the next round of ICP, similar to VICP [28].

E. Map Update

1) *Depth Fusion*: Once the ICP procedure has converged, we can undistort the current sweep using the optimized local trajectory and update the pano. This is achieved by projecting every pixel from the sweep to the pano using Eq. 3. Although in principle one could maintain a probabilistic depth filter for each pixel and perform recursive Bayesian updates [29] given the new depth, we found that in practice, the similarity filter used in [22] worked exceptionally well with very low computation and storage overhead. We keep a counter k alongside the depth value for each pixel in the pano. If the new depth d' is close enough to the stored depth d , we do a weighted average update and increment the counter by 1, saturating at k_{\max} .

$$d \leftarrow \frac{k \cdot d + d'}{k + 1}, \quad k \leftarrow \min(k_{\max}, k + 1) \quad (6)$$

We otherwise treat the new depth as an outlier and simply decrements the counter by 1 without modifying the current value. If k reaches 0, we replace d with d' . This simple depth fusion strategy produces smooth depth surfaces as is evident in Fig. 5. It also makes our map resilient to ephemeral objects, while still being able to adapt to long-term environment changes. For example, a car driving across the lidar will typically leave a trail of ghost points in a point cloud map, but it will not be registered into the pano unless it has stopped moving for a long enough time.

2) *Rendering New Panoramas*: As the sensor moves away from the pano, the number of matches between the two will gradually decrease. This is due to the projective nature of range images, where data association is affected by occlusions and non-overlapping FOVs. Therefore, we need to move the pano to a new position in order to retain a healthy number of matches for ICP.

The decision on whether to relocate the pano is made by looking at the matching quality Q , which is defined as the ratio between the number of final matches and matching

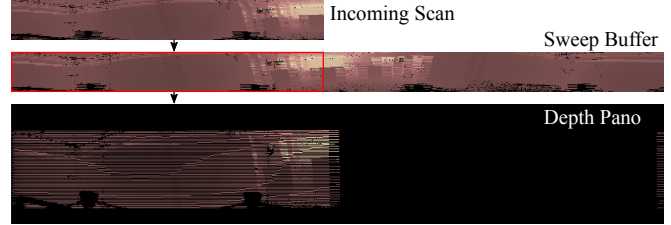


Fig. 6: Illustration of how partial sweeps are handled. The incoming partial sweep is pushed into a sweep buffer. The part being ejected from the buffer is added to the pano.

candidates. This number essentially reflects the amount of non-occluding overlap between the sweep and the pano. Once Q drops below a certain threshold (0.9 by default), we will render a new pano at the current location. If IMU measurements are available and motion in roll and pitch is limited, the new pano will be placed in a gravity aligned frame. Since we do not have dense depth information in the new location, we do a forward warping from the old pano to the new one. This will naturally result in many holes in the new pano, but this can be alleviated by immediately incorporating the current sweep. The rendering process is executed at a much lower rate, since it is only triggered when the two viewpoints start to deviate from each other.

IV. IMPLEMENTATION

A. Processing Partial Sweeps

To handle partial sweeps, we maintain a circular buffer for a full sweep, and push incoming partial sweeps into the buffer as they arrive. The part of the buffer being ejected is immediately fused with the pano using the current state estimate. This is shown in Fig. 6, where the ejected part is outlined in red. However, performing ICP with a partial sweep is challenging because the smaller the size, the more likely it is to encounter degeneracy. Therefore, we use the entire sweep in the buffer for this task, which has 360° FOV. This adaptation is key to minimizing latency. For example, if we process half of a sweep at a time, this reduces the sensor integration time to 50 ms (assuming a 10 Hz spinning rate). It also halves the feature detection and pano update time, as they only need to process half of the data. The ICP time remains unchanged, since it always tries to align the full sweep in the buffer to the pano. This essentially increases the odometry frequency to 20 Hz. One could further divide the sweep into smaller chunks, but there exists a lower bound on how narrow a partial sweep can be handled without dropping data, which is subject to the ICP processing time. In practice, our system can handle 1/8th of a sweep which produces odometry at 80 Hz.

B. Memory Layout and Parallelization

Our implementation follows a data-oriented design [30] and is optimized for cache-locality and parallelism. We only use array-based data structures and pre-allocate all storage ahead of time. There is no dynamic allocation occurring at runtime within our system, which makes it favorable for

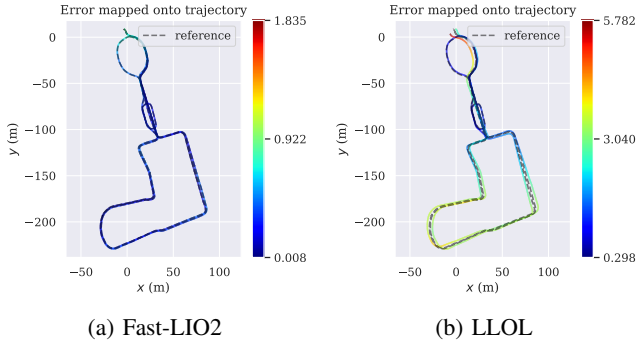


Fig. 7: Trajectory error plots of Fast-LIO2 and LLOL on Newer College dataset sequence 1.

embedded applications. Specifically, we only need to allocate enough storage for a full sweep, a feature grid, two **panos** and various arrays for the solver and the local trajectory. Together they require no more than 5-10MB of storage.

The projective data association is also significantly faster compared to systems that leverage even a carefully designed KD-tree [31]. A tree data structure requires frequent node allocation and pointer chasing during search and insertion. Without advanced memory management or allocator support, almost every node access is a cache miss, which severely hinders performance on modern processors. On the other hand, the projection operation is constant time, which is conceptually similar to a hash-table lookup.

Finally, almost every step of our system can be parallelized, since we mostly operate on images. We choose a single row in both the sweep and the pano as our atomic work unit, and use a task-based threading library [32] for scheduling. A finer grain size of a single pixel is possible, but it requires additional synchronization overhead to avoid false-sharing. Rendering a new **pano** is carried out in the background via double buffering (<10 ms in a single thread on Intel CPU), which does not interfere with the odometry.

V. RESULTS

We evaluate both the accuracy and runtime performance of our proposed system. For comparison we choose Fast-LIO2 [6], which is a state-of-the-art **lidar**-inertial odometry with an open-source implementation¹. We use their default configuration for Ouster **lidar**² with slightly tuned imu noise parameters. For our system, unless otherwise specified, we use a pano of size 256×1024 , and a cell size of 2×16 .

A. Odometry Accuracy

1) *Newer College Dataset*: As our system consumes lidar packets, this limits our choice of publicly available datasets to evaluate on. The Newer College dataset [33] provides raw lidar packets along with ground truth trajectories. We evaluate on two sequences: *01-short-experiment (NC01)* and *05-quad-with-dynamics (NC05)*, both collected with a handheld

¹https://github.com/hku-mars/FAST_LIO

²<https://ouster.com/products/os1-lidar-sensor>

TABLE I: Translational APE and RPE on NC01.

Newer College Sequence 1 Segment	t_{start}	t_{end}	Fast-LIO2		LLOL	
			APE	RPE	APE	RPE
1	25	340	0.363	0.214	0.396	0.283
2	340	705	0.165	0.112	0.499	0.214
3	705	1115	0.277	0.171	0.706	0.250
4	1115	1500	0.311	0.121	0.912	0.238

TABLE II: Translational APE and RPE on NC05.

Newer College Sequence 5 Segment	t_{start}	t_{end}	Fast-LIO2		LLOL	
			APE	RPE	APE	RPE
1	25	100	0.104	0.172	0.130	0.328
2	100	200	0.136	0.206	0.183	0.319
3	200	300	0.102	0.122	0.178	0.258
4	300	400	0.162	0.119	0.262	0.288

sensor platform at normal walking pace. Note that *NC05* features 4 loops with increasingly aggressive motion. Within each sequence, the sensor is stopped at various locations for a short while. This creates well-defined segments which allows for sub-trajectory evaluation. We report results on these segments in Table I and II, and visualize the full trajectory of *NC01* in Fig. 7.

We report the translational part of Absolute Pose Error (APE) and Relative Pose Error (RPE) metrics, both generated using the *evo* [34] package. APE measures the difference in pose between the reference and the estimated trajectory. We use Umeyama alignment [35] as a pre-processing step to align the trajectories for all methods. RPE compares pairwise relative pose within a small window (1 m), which can be used to quantify odometry drift.

Fast-LIO2 outperforms LLOL in both sequences. This is because part of the Newer College dataset was collected in a park with many trees and few man-made structures. This results in reduced planar features for our system. In addition, the sensor went under tree canopies several times, the heavy occlusion triggered more frequent rendering of the **pano**, thus causing extra drift.

2) *Our Own Dataset*: In addition to the Newer College dataset, we also collect our own for evaluation. We acquire the dataset with a handheld Ouster OS1 Gen2 sensor running at 10Hz with 1024 firings per sweep. Following [36], we come back to the starting point after a loop, and the difference between the first and the last pose can be used to evaluate odometry drift without ground truth. We test in four distinct scenarios: a small loop, a large loop, an open space trajectory and an aggressive motion trajectory. Quantitative results are shown in Table III. We report the total distance estimated by each system and their final positional error. The drift is calculated as the quotient of the two. Both systems work well on the first 3 sequences with normal walking motion, but Fast-LIO2 failed to converge on the last one with aggressive rotation. LLOL is able to achieve $<1\%$ drift on all sequences. Qualitative results are shown in Fig. 8.

B. Runtime and Latency

We benchmark both LLOL and Fast-LIO2 on a desktop CPU (Intel i7-6700K@4.2GHz) as well as an embedded

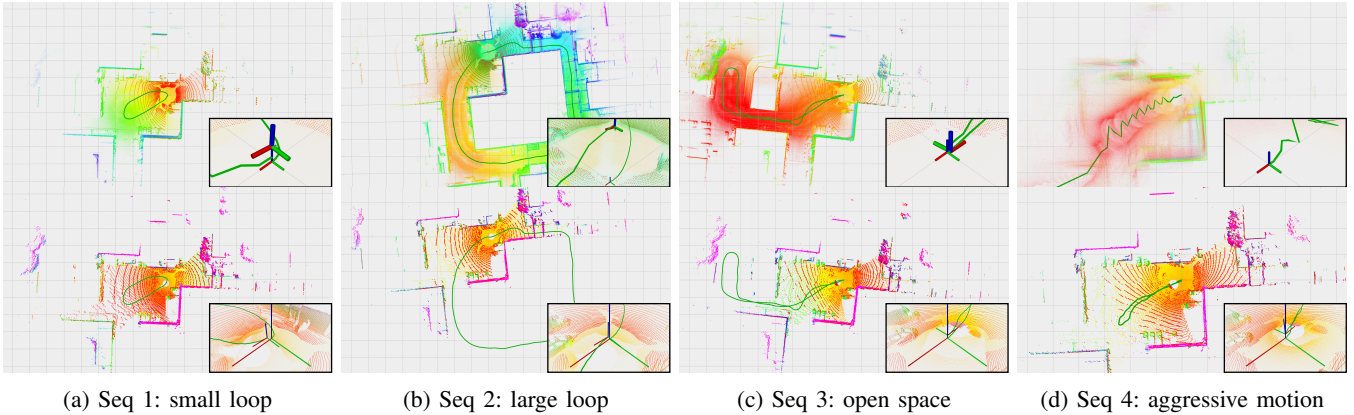


Fig. 8: Qualitative results of Fast-LIO2 (top) and LLOL (bottom) on our own datasets.

TABLE III: Trajectory drift of Fast-LIO2 and LLOL on our own dataset.

Seq.	Fast-LIO2			LLOL		
	Distance	Error	Drift	Distance	Error	Drift
1	69.53	0.91	1.31%	64.88	0.38	0.58%
2	257.52	6.53	2.54%	244.00	0.25	0.10%
3	208.20	0.21	0.10%	201.00	0.52	0.26%
4	869.87	358.1	41.2%	63.07	0.43	0.68%

one (ARMv8.2@2.2GHz, NVIDIA Xavier) under single and multi-threaded settings. In addition, we conducted experiments on both indoor and outdoor datasets. The outdoor environment is roughly twice the size of the indoor one. This is to demonstrate the effect of workspace sizes on each system. For Fast-LIO2, we report the total time in the same way as the original paper. For LLOL, we record time from the (partial) sweep arrival to the end of pano update. The pano rendering only runs infrequently in the background and is not included in the timing results.

Runtime results are shown in Table IV. We see that LLOL is in general much faster than Fast-LIO2, with sub-millisecond processing time in some cases. Fast-LIO2 exhibits large variance in runtime between indoor and outdoor environments, while LLOL runs in near constant time regardless of workspace size. We also visualize the per-frame runtime on NC01 in Fig. 9. While LLOL maintains a fairly stable performance over the entire sequence, Fast-LIO2 displays inconsistent results, with intermittent bursts up to 100ms. The latency of each method can be computed by adding the sensor integration time with the runtime. For example, running LLOL with a quarter sweep will result in an average latency of 28.37 ms on Xavier with a single thread, as opposed to 189.81 ms for Fast-LIO2.

Finally, our system running on embedded CPUs compares favourably to UPSLAM [22] (5 ms on Xavier) which requires a GPU. LITAMIN2 [16] (5 ms on Intel CPU) can also achieve similar speed as ours, but the lack of open source implementations precludes a fair comparison.

VI. CONCLUSIONS

In this paper, we present a low-latency odometry system for spinning lidars. It has comparable accuracy and drift

TABLE IV: Runtime comparison of Fast-LIO2 vs LLOL on different types of processors under single and multi-threaded settings for both indoor (top) and outdoor (bottom) environments. Results are averaged within the entire sequence.

method	Runtime [ms]		Xavier (ARMv8.2)		Intel (i7-6700K)	
	sweep (ms)		single	multi (8)	single	multi (8)
Fast-LIO2	full (100)	44.59	27.13	22.22	21.09	
LLOL	full (100)	12.56	4.46	5.24	1.93	
LLOL	1/2 (50)	6.87	3.02	3.02	1.29	
LLOL	1/4 (25)	4.32	2.30	1.87	0.94	
Fast-LIO2	full (100)	89.81	34.40	42.67	28.63	
LLOL	full (100)	10.15	3.77	3.89	1.56	
LLOL	1/2 (50)	5.68	2.55	2.33	1.07	
LLOL	1/4 (25)	3.37	1.89	1.46	0.77	

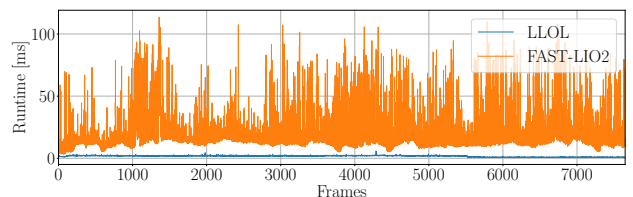


Fig. 9: Per-frame runtime of Fast-LIO2 and LLOL on NC01, measured on Intel CPU with 8 threads. LLOL has an average runtime of 1.70 ± 0.55 ms. Fast-LIO2 has an average runtime of 21.73 ± 16.50 ms.

to a state-of-the-art lidar odometry system [6], but runs an order of magnitude faster. The decision to handle partial sweeps significantly boosts the odometry update frequency of our system compared to approaches operating at the nominal rotational rate of the lidar sensor. A key enabler of our fast implementation is the use of depth panoramas as our local map representation, this affords us constant time search and update complexity across different environment scales. Our odometry system offers a high data throughput combined with a low memory footprint, these features make it suitable for deployment on resource constrained platforms. We open source our implementation as a contribution to the community.

REFERENCES

- [1] J. Zhang and S. Singh, "Visual-lidar odometry and mapping: low-drift, robust, and fast," *2015 IEEE International Conference on Robotics and Automation (ICRA)*, pp. 2174–2181, 2015.
- [2] T. Shan, B. Englot, C. Ratti, and D. Rus, "Lvi-sam: Tightly-coupled lidar-visual-inertial odometry via smoothing and mapping," *ArXiv*, vol. abs/2104.10831, 2021.
- [3] S. Zhao, H. Zhang, P. Wang, L. Nogueira, and S. Scherer, "Super odometry: Imu-centric lidar-visual-inertial estimator for challenging environments," *ArXiv*, vol. abs/2104.14938, 2021.
- [4] D. Frossard, S. Suo, S. Casas, J. Tu, R. Hu, and R. Urtasun, "Stroke: Streaming object detection from lidar packets," *ArXiv*, vol. abs/2011.06425, 2020.
- [5] W. Han, Z. Zhang, B. Caine, B. Yang, C. Sprunk, O. Alsharif, J. Ngiam, V. Vasudevan, J. Shlens, and Z. Chen, "Streaming object detection for 3-d point clouds," *ArXiv*, vol. abs/2005.01864, 2020.
- [6] W. Xu, Y. Cai, D. He, J. Lin, and F. Zhang, "Fast-lid2: Fast direct lidar-inertial odometry," *ArXiv*, vol. abs/2107.06829, 2021.
- [7] J. Zhang and S. Singh, "Loam: Lidar odometry and mapping in real-time," in *Robotics: Science and Systems*, 2014.
- [8] T. Shan and B. Englot, "Lego-loam: Lightweight and ground-optimized lidar odometry and mapping on variable terrain," *2018 IEEE/RSJ International Conference on Intelligent Robots and Systems (IROS)*, pp. 4758–4765, 2018.
- [9] Z. Liu and F. Zhang, "Balm: Bundle adjustment for lidar mapping," *IEEE Robotics and Automation Letters*, vol. 6, pp. 3184–3191, 2021.
- [10] C. Park, P. Moghadam, S. Kim, A. Elfes, C. Fookes, and S. Sridharan, "Elastic lidar fusion: Dense map-centric continuous-time slam," *2018 IEEE International Conference on Robotics and Automation (ICRA)*, pp. 1206–1213, 2018.
- [11] C. Park, P. Moghadam, J. Williams, S. Kim, S. Sridharan, and C. Fookes, "Elasticity meets continuous-time: Map-centric dense 3d lidar slam," *ArXiv*, vol. abs/2008.02274, 2020.
- [12] J. Behley and C. Stachniss, "Efficient surfel-based slam using 3d laser range data in urban environments," in *Robotics: Science and Systems*, 2018.
- [13] J. Quenzel and S. Behnke, "Real-time multi-adaptive-resolution-surfel 6d lidar odometry using continuous-time trajectory optimization," *ArXiv*, vol. abs/2105.02010, 2021.
- [14] M. Yokozuka, K. Koide, S. Oishi, and A. Banno, "Litamin: Lidar-based tracking and mapping by stabilized icp for geometry approximation with normal distributions," *2020 IEEE/RSJ International Conference on Intelligent Robots and Systems (IROS)*, pp. 5143–5150, 2020.
- [15] A. V. Segal, D. Hähnel, and S. Thrun, "Generalized-icp," in *Robotics: Science and Systems*, 2009.
- [16] M. Yokozuka, K. Koide, S. Oishi, and A. Banno, "Litamin2: Ultra light lidar-based slam using geometric approximation applied with kl-divergence," *ArXiv*, vol. abs/2103.00784, 2021.
- [17] K. Li, M. Li, and U. Hanebeck, "Towards high-performance solid-state-lidar-inertial odometry and mapping," *IEEE Robotics and Automation Letters*, vol. 6, pp. 5167–5174, 2021.
- [18] J. Lin and F. Zhang, "Loam livox: A fast, robust, high-precision lidar odometry and mapping package for lidars of small fov," *2020 IEEE International Conference on Robotics and Automation (ICRA)*, pp. 3126–3131, 2020.
- [19] T. Shan, B. Englot, D. Meyers, W. Wang, C. Ratti, and D. Rus, "Lio-sam: Tightly-coupled lidar inertial odometry via smoothing and mapping," *2020 IEEE/RSJ International Conference on Intelligent Robots and Systems (IROS)*, pp. 5135–5142, 2020.
- [20] H. Ye, Y. Chen, and M. Liu, "Tightly coupled 3d lidar inertial odometry and mapping," *2019 International Conference on Robotics and Automation (ICRA)*, pp. 3144–3150, 2019.
- [21] W. Xu and F. Zhang, "Fast-lid: A fast, robust lidar-inertial odometry package by tightly-coupled iterated kalman filter," *IEEE Robotics and Automation Letters*, vol. 6, pp. 3317–3324, 2021.
- [22] A. Cowley, I. D. Miller, and C. J. Taylor, "Upslam: Union of panoramas slam," *ArXiv*, vol. abs/2101.00585, 2021.
- [23] C. J. Taylor, A. Cowley, R. Kettler, K. Ninomiya, M. Gupta, and B. Niu, "Mapping with depth panoramas," *2015 IEEE/RSJ International Conference on Intelligent Robots and Systems (IROS)*, pp. 6265–6272, 2015.
- [24] G. Kim and A. Kim, "Scan context: Egocentric spatial descriptor for place recognition within 3d point cloud map," *2018 IEEE/RSJ International Conference on Intelligent Robots and Systems (IROS)*, pp. 4802–4809, 2018.
- [25] H. Wang, C. Wang, and L. Xie, "Intensity scan context: Coding intensity and geometry relations for loop closure detection," *2020 IEEE International Conference on Robotics and Automation (ICRA)*, pp. 2095–2101, 2020.
- [26] J. Serafin and G. Grisetti, "Nlcp: Dense normal based point cloud registration," *2015 IEEE/RSJ International Conference on Intelligent Robots and Systems (IROS)*, pp. 742–749, 2015.
- [27] C. Forster, L. Carlone, F. Dellaert, and D. Scaramuzza, "On-manifold preintegration for real-time visual-inertial odometry," *IEEE Transactions on Robotics*, vol. 33, pp. 1–21, 2017.
- [28] S. Hong, H. Ko, and J. Kim, "Vicp: Velocity updating iterative closest point algorithm," *2010 IEEE International Conference on Robotics and Automation*, pp. 1893–1898, 2010.
- [29] C. Forster, M. Pizzoli, and D. Scaramuzza, "Svo: Fast semi-direct monocular visual odometry," *2014 IEEE International Conference on Robotics and Automation (ICRA)*, pp. 15–22, 2014.
- [30] R. Fabian, *Data-Oriented Design: Software Engineering for Limited Resources and Short Schedules*, 2018.
- [31] Y. Cai, W. Xu, and F. Zhang, "ikd-tree: An incremental k-d tree for robotic applications," *ArXiv*, vol. abs/2102.10808, 2021.
- [32] M. Voss, R. Asenjo, and J. Reinders, *Pro TBB: C++ Parallel Programming with Threading Building Blocks*, 1st ed. USA: Apress, 2019.
- [33] M. Ramezani, Y. Wang, M. Camurri, D. Wisth, M. Mattamala, and M. Fallon, "The newer college dataset: Handheld lidar, inertial and vision with ground truth," *2020 IEEE/RSJ International Conference on Intelligent Robots and Systems (IROS)*, pp. 4353–4360, 2020.
- [34] M. Grupp, "evo: Python package for the evaluation of odometry and slam," <https://github.com/MichaelGrupp/evo>, 2017.
- [35] S. Umeyama, "Least-squares estimation of transformation parameters between two point patterns," *IEEE Transactions on Pattern Analysis & Machine Intelligence*, vol. 13, no. 04, pp. 376–380, 1991.
- [36] J. Engel, V. Usenko, and D. Cremers, "A photometrically calibrated benchmark for monocular visual odometry," *ArXiv*, vol. abs/1607.02555, 2016.